International Journal of Heat and Mass Transfer 232 (2024) 125929

Contents lists available at ScienceDirect

International Journal of Heat and Mass Transfer

journal homepage: www.elsevier.com/locate/hmt

Effects of rough surfaces on annular centrifugal Rayleigh–Bénard convection

Fan Xu [a,c], Jun Zhong [d,e], Jinghong Su [d,e], Bidan Zhao [b,c], Yurong He [a,*], Chao Sun [d,e,*], Junwu Wang [b,c,**]

[a] School of Energy Science and Engineering, Harbin Institute of Technology, Harbin, 150001, PR China
[b] College of Mechanical and Transportation Engineering, China University of Petroleum, Beijing 102249, PR China
[c] State Key Laboratory of Mesoscience and Engineering, Institute of Process Engineering, Chinese Academy of Sciences, Beijing 100190, PR China
[d] New Cornerstone Science Laboratory, Center for Combustion Energy, Key Laboratory for Thermal Science and Power Engineering of Ministry of Education, Department of Energy and Power Engineering, Tsinghua University, Beijing 100084, PR China
[e] Department of Engineering Mechanics, School of Aerospace Engineering, Tsinghua University, Beijing 100084, PR China

ARTICLE INFO

Keywords:
Direct numerical simulation
Annular centrifugal Rayleigh–Bénard convection
Rough surfaces
Heat transport enhancement
Zonal flow

ABSTRACT

Two-dimensional direct numerical simulations are performed to explore the effects of rough surfaces on the temperature fields, heat transport, and zonal flow in the annular centrifugal Rayleigh–Bénard convection (ACRBC) with cold inner and hot outer cylinders co-rotating axially, up to a Rayleigh number of $Ra = 4.7 \times 10^9$. Three combinations of roughness are considered, that is, two rough surfaces (Case A), rough-inner/smooth-outer (Case B) and smooth-inner/rough-outer (Case C). It is shown that, the rough walls cause a bias in the temperature fields towards the values set on the rough walls at high *Ra*, while have a minimal impact at low *Ra*. This effect can be attributed to the rough walls promoting the generation and detachment of plumes, which act as the primary heat carriers in turbulent convective heat transfer. Furthermore, the presence of rough surfaces leads to enhanced heat transport at high Rayleigh numbers. Notably, two universal regimes are distinguished by the critical Rayleigh number $Ra_c \approx 10^9$: in regime I, where roughness elements protrude through the thermal boundary layer (BL), heat transport is significantly enhanced, resulting in a considerable increase in scaling exponent; in regime II, the scaling exponent reaches a saturation point, returning to a value similar to the smooth case. Similar findings are also observed in the classical Rayleigh–Bénard convection (Zhu et al., 2017). The decrease in scaling exponent can be attributed to the intense mixing caused by secondary vortices within the roughness elements, leading to a thin and uniformly distributed thermal BL along the rough surfaces, resembling the behavior observed in the smooth case. It is also found that roughness on the outer wall promotes the emergence of zonal flow, while roughness on the inner wall weakens it. These findings provide valuable insights into the effect of wall roughness on temperature fields, heat transport, and zonal flow in ACRBC.

1. Introduction

Turbulent thermal convection plays an important role in a range of processes in astrophysical and geophysical systems. Examples are convection in the oceans and atmosphere, where the underlying surfaces are generally not smooth. An ideal model for the study of turbulent thermal convection is classical Rayleigh–Bénard convection (RBC), where a fluid is confined between two flat horizontal plates heated from the bottom and cooled from the top. This has been studied extensively in the past few decades (see Ahlers et al. [1], Lohse and Xia [2], Chillà and Schumacher [3] for reviews). When the system undergoes axial rotation, the classical RBC transitions to rotating Rayleigh–Bénard convection (RRBC) as described in a comprehensive review by Ecke and Shishkina [4]. In RBC, the driving force is buoyancy, while in RRBC, the centrifugal and Coriolis forces are also introduced.

The core issues for thermal turbulence studies are the flow dynamics and heat transfer in a wide range of the control parameters. The relation between the heat transport, the Nusselt number *Nu* (the ratio of total heat flux to conductive heat flux) and the Rayleigh number *Ra* (the ratio of buoyancy to viscous forces) can be expressed as $Nu = ARa^{\beta}$, A is the prefactor and β is the power law index. Recently, an annular centrifugal Rayleigh–Bénard convection (ACRBC) system with cold inner and hot outer cylinders corotating axially, a novel system for studying Rayleigh–Bénard convection, has been proposed [5–10]. Utilizing the robust centrifugal force generated by

* Corresponding authors.
** Corresponding author at: College of Mechanical and Transportation Engineering, China University of Petroleum, Beijing 102249, PR China.
E-mail addresses: rong@hit.edu.cn (Y. He), chaosun@tsinghua.edu.cn (C. Sun), jwwang@cup.edu.cn (J. Wang).

https://doi.org/10.1016/j.ijheatmasstransfer.2024.125929
Received 11 May 2024; Received in revised form 30 June 2024; Accepted 2 July 2024
Available online 15 July 2024

rapid rotation, the thermal driving force in ACRBC can be significantly intensified, allowing for the attainment of higher Rayleigh numbers and promoting thermal convection to the ultimate regime [11]. The thermal convection observed in a rapidly rotating cylindrical annulus serves as a valuable model for studying flows in planetary cores and stellar interiors [12–16], adding to the advantages of this system.

The heat transfer and flow dynamics in ACRBC are different from those in classical RBC, owing to the different curvatures of the inner and outer cylinder and the Coriolis force. According to the experimental and numerical study conducted by Jiang et al. [5], it was observed that the heat transfer efficiency decreases with increasing Coriolis force. This decline can be attributed to the weakening of axial flow caused by the constraints due to the Taylor–Proudman theorem [17,18] under strong Coriolis forces. Consequently, when subjected to strong Coriolis forces (inverse Rossby numbers $Ro^{-1} \geq 10$), the flow in ACRBC becomes nearly two-dimensional, lacking substantial axial flow. This alteration in flow pattern results in reduced heat transport compared to the regime at low Ro^{-1}. Furthermore, through a comparison of two- and three-dimensional simulation results, the study confirmed that the aspect ratio of ACRBC has minimal impact on heat transfer at high inverse Rossby numbers ($Ro^{-1} \geq 10$). In addition, they found that four pair convection rolls distribute in the cell and revolve around the rotating center in the prograde direction of the system, which is called as 'zonal flow'. In the later study, Jiang et al. [11] evidenced that the ultimate regime occurs in ACRBC when $Ra \geq 10^{11}$, which is three orders of magnitude lower than $Ra \approx 10^{14}$ reported in classical RBC [19,20]. Furthermore, by using different working fluids with Prandtl numbers (Pr) of 4.3 and 10.4, they observed a weak dependence of heat transfer on Pr, consistent with previous studies in the Pr range [4, 10.7] in classical RBC [21,22]. Wang et al. [7] focused on the effects of radius ratio on flow dynamics, heat transport and temperature field in ACRBC and found that the zonal flow becomes weaker with increasing radius ratio η, but the heat transport efficiency increases with η. They also reported that the bulk temperature deviates from the arithmetic mean temperature and the deviation increases as η decreases. It has been widely accepted that any wall roughness increases heat transfer once the thermal boundary layer (BL) thickness is smaller than the height of the roughness in the Rayleigh–Bénard (RB) system [23–27]. To date, all studies on ACRBC have considered smooth wall surfaces. How the temperature fields, heat transfer and flow dynamics change in ACRBC with the introduction of roughness? In the present study, we will answer these questions.

In this article, direct numerical simulations (DNS) of ACRBC with rough surfaces are carried out to study how different combinations of roughness affect the global heat transport as well as local flow behavior. The manuscript is organized as follows. In Section 2, the numerical settings are described. In Section 3, the temperature fields and the relations between the Nusselt number and the Rayleigh number with different roughness cases are shown, the mechanism behind the differences in heat transport is then explained. The zonal flow and local flow behavior are also analyzed. Finally, conclusions are drawn in Section 4.

2. Numerical settings

2.1. Governing equation

An annular centrifugal RB cell bounded by cold inner and hot outer cylinders, which rotate co-axially as shown in Fig. 1(*a*), is studied. Our objective is to explore the impact of different combinations of roughness on ACRBC. As depicted in Fig. 1(*b*), we consider three specific combinations of rough surfaces, each characterized by a uniform roughness element height of $\delta = 0.1L$. Here, L is the gap width without roughness. In 'Case A', the inner cylinder is equipped with sixteen isosceles right triangles that are equally distributed in the azimuthal direction, while the outer cylinder features thirty-two triangles. For 'Case B', we maintain the same number of roughness elements as in Case A on the inner cylinder, but the outer wall remains smooth. Conversely, 'Case C' involves a smooth inner cylinder combined with a rough outer cylinder, where the number of roughness elements matches that of Case A.

The motion and heat transfer of the fluid under the Oberbeck-Boussinesq approximation is governed by the non-dimensional Navier–Stokes-Fourier equations in a rotating frame [7]:

$$\nabla \cdot \boldsymbol{u} = 0, \tag{1}$$

$$\frac{\partial \boldsymbol{u}}{\partial t} + \nabla \cdot (\boldsymbol{u}\boldsymbol{u}) = -\nabla p - Ro^{-1}\boldsymbol{e}_z \times \boldsymbol{u} + \sqrt{\frac{Pr}{Ra}}\nabla^2 \boldsymbol{u} - \theta \frac{2(1-\eta)}{1+\eta}\boldsymbol{r}, \tag{2}$$

$$\frac{\partial \theta}{\partial t} + \nabla \cdot (\boldsymbol{u}\theta) = \frac{1}{\sqrt{RaPr}}\nabla^2 \theta, \tag{3}$$

where $\boldsymbol{u}$ is the velocity vector, t is the time, p is the pressure, $\boldsymbol{e}_z$ is the unit vector along the axial direction, θ is the temperature, and η is the radius ratio. The equations are normalized using the gap width (without roughness) $L = R_o - R_i$ for length, the temperature difference between the hot outer cylinder and the cold inner cylinder $\Delta = \theta_{hot} - \theta_{cold}$ for temperature, the free-fall velocity $\boldsymbol{U} = \sqrt{\omega^2((R_i + R_o)/2)\alpha\Delta L}$ for velocity, and L/U for time. Here, ω donates the angular velocity of the system, and α is the coefficient of thermal expansion of the fluid. In the coordinate system r, φ, z refer to the wall-normal (radial), streamwise (azimuthal) and spanwise (axial) directions. In the following, we define the non-dimensional radius R^* to be $R^* = (R - R_i)/(R_o - R_i)$.

From the above non-dimensional equations, it can be seen that there are four dimensionless control parameters in ACRBC. The Rayleigh number (buoyancy-driven strength)

$$Ra = \omega^2(R_i + R_o)\alpha\Delta L^3/(2\nu\kappa), \tag{4}$$

and the Prandtl number (fluid physical property)

$$Pr = \nu/\kappa, \tag{5}$$

as in classical RBC, where ν and κ are the kinematic viscosity and thermal diffusivity of the fluid, respectively. Two additional control parameters are the inverse Rossby number

$$Ro^{-1} = 2\omega L/U, \tag{6}$$

which measures the effects of Coriolis force, and the radius ratio that measures the geometric property

$$\eta = R_i/R_o. \tag{7}$$

In addition, the key response parameter is the Nusselt number measuring the efficiency of heat transport

$$Nu = J/J_{con} = (\langle u_r\theta\rangle_{\varphi,z,t} - \kappa\partial_r\langle\theta\rangle_{\varphi,z,t})/(\kappa\Delta(r \cdot ln(\eta))^{-1}), \tag{8}$$

where J, J_{con}, u_r, and θ are the total heat flux, the heat flux through pure thermal conduction, the radial velocity and the temperature of a certain point, respectively. Here, $\langle ... \rangle_{\varphi,z,t}$ denotes averaging over a cylindrical surface (averaging over the axial and azimuthal directions) with constant distance from the axis and over time. Note that the expression of conductive heat flux in cylindrical geometry is slightly different from that in classical RBC, the detailed derivation process can be found in our previous study [7].

2.2. Direct numerical simulations

Eqs. (1)–(3) are solved using a second-order-accuracy, colocated finite-volume method in the Cartesian coordinate system, using OpenFOAM as the computational platform. The rough elements are dealt with a second-order-accuracy immersed boundary method [28,29]. According to Jiang et al. [5], due to the constraint of Taylor–Proudman theorem, the flow is nearly two-dimensional (without axial flow) at

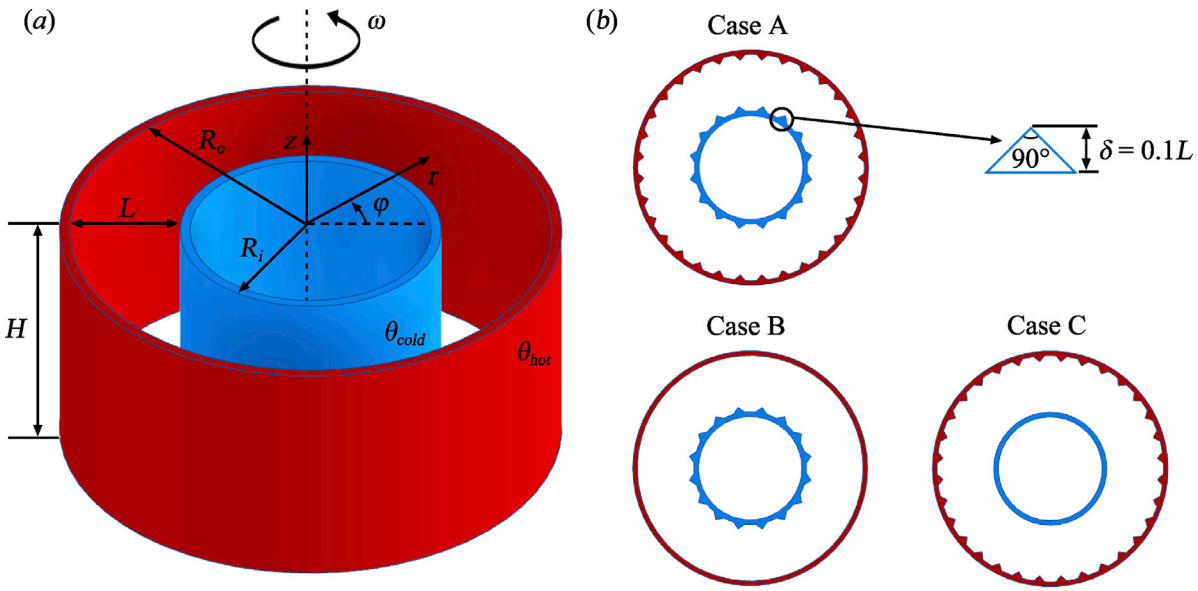

Fig. 1. Schematic view of the annular centrifugal Rayleigh–Bénard convection system and the different combinations of roughness. (*a*) Three-dimensional view, here ω is the angular velocity of the system. All cases in this paper set the angular velocity $\omega > 0$, that is, the system rotates anticlockwise. Here R_i, R_o, H and L are the outer radius of the inner cylinder, the inner radius of the outer cylinder, the height of the cylindrical annulus, and the gap width between the two cylinders, respectively. θ_{hot} and θ_{cold} denote the temperature of the outer and inner walls. (*b*) Three different combinations of roughness: Case A, where both cylinders are rough; Case B, where the inner cylinder is rough but the outer one is smooth; and Case C, where the outer cylinder is rough but the inner one is smooth. For the rough walls, the rough elements consist of sixteen equidistantly positioned isosceles right triangles on the inner cylinder wall and thirty-two equidistantly positioned isosceles right triangles on the outer cylinder wall. The height of the rough elements is $0.1L$.

high Ro^{-1} (≥ 10). Therefore, two-dimensional direct numerical simulations (2D-DNS) are carried out in the present study with a fixed inverse Rossby number $Ro^{-1} = 20$. No-slip boundary condition is used for velocity and constant temperature boundary condition is used for the temperature at two cylinder walls.

Adequate resolutions are ensured for all simulations and we have performed posterior checks of spatial and temporal resolutions to guarantee the resolution of all relevant scales. The ratios of maximum grid spacing Δ_g to the Kolmogorov scale estimated by the global criterion $\eta_K = LPr^{1/2}/[Ra(Nu-1)]^{1/4} \cdot [(1+\eta)ln(\eta)/2(\eta-1)]^{1/4}$ [5] is smaller than 1.0 ($\Delta_g/\eta_K < 1.0$), and the Batchelor scale $\eta_B = \eta_K Pr^{-1/2}$ [30] is smaller than 2.0 ($\Delta_g/\eta_B < 2.0$), as shown in Table 1. Furthermore, the grid is uniform in the azimuthal direction, and refined near the inner and outer cylindrical walls in the radial direction to ensure the spatial resolution within boundary layers (BLs). There are at least 8 grid points inside thermal BLs and 10 grid points inside viscous BLs. The temporal term is discretized using the second-order backward scheme and the convective term is discretized using a second-order total variation diminishing (Vanleer) scheme. All simulations are achieved using a fixed time step based on the Courant–Friedrichs–Lewy (CFL) criterion and The CFL number is less than 0.7 in all simulations. The simulations are run over enough time (80 free-fall time) after the system has reached the statistically stationary state (100 free-fall time) to obtain good statistical convergence. The relative difference of *Nu* based on the first and second halves ($\epsilon_{Nu} = |\langle Nu\rangle_{0-T/2} - \langle Nu\rangle_{T/2-T})|/Nu$) of the simulations is less than 1% as shown in Table 1.

The motivation behind this study is to investigate how roughness influences the flow dynamics and heat transport in the ACRBC system. While there are various options for roughness shapes, we specifically focus on the isosceles right triangular rib as the simplest geometry model to analyze its impact on the statistical properties of turbulent ACRBC. Our main research question aims to understand how the presence of roughness elements affects both the global transport and local flow statistics in the ACRBC turbulence. The radius ratio of $\eta = 0.5$ is set to make a direct comparison with previous results [5,11]. In all simulations, the Prandtl number *Pr* is fixed at 4.3, corresponding to the working fluids of water at 40 °C. As mentioned earlier, the inverse Rossby number is fixed at $Ro^{-1} = 20$ to enable the exploration of Rayleigh number from $Ra = 1.0\times10^6$ up to $Ra = 4.7\times10^9$ using 2D-DNS.

3. Results

3.1. Temperature fields

We begin our analysis by comparing the instantaneous temperature fields at two distinct Rayleigh numbers: $Ra = 10^6$, and $Ra = 10^9$, considering three different combinations of rough walls (Case A, Case B, and Case C) as well as smooth wall, as illustrated in Fig. 2. At the low Rayleigh number $Ra = 10^6$ (Fig. 2*a*), the temperature fields exhibit remarkable similarity independent of wall roughness. Notably, for rough walls, it is important to highlight that at this low Rayleigh number, most of the roughness elements are submerged within the thermal boundary layer. This results in the formation of cold plumes along the inner wall and hot plumes along the outer wall, primarily originating from the tips of the roughness elements and subsequently detaching in the direction of the convection rolls. However, in the regions between the roughness elements, the flow is dominated by viscosity. At the large Rayleigh number $Ra = 10^9$ (Fig. 2*b*), the situation becomes more intricate compared to $Ra = 10^6$. A notable observation is that the roughness elements extend beyond the thermal BL, resulting in the generation of plumes not only at the tips but also within the cavity regions. Within these regions, the detached plumes vigorously mix the fluid, leading to increased turbulence in the flow. These findings align with studies conducted on classical RBC with similar effective roughness height [26,31]. However, in the present study, the roughness has a significant impact on the temperature fields at a relatively lower Rayleigh number (approximately one order of magnitude lower). This difference can be attributed to the influence of Coriolis force in ACRBC, which can enhance thermal convection [6]. This leads to a thinner thermal BL in ACRBC compared to classical RBC at the same Rayleigh number. As a result, the rough elements have the ability to influence the flow and temperature fields in ACRBC, even at a relatively lower *Ra*. Additionally, as depicted in Fig. 2(*b*), the

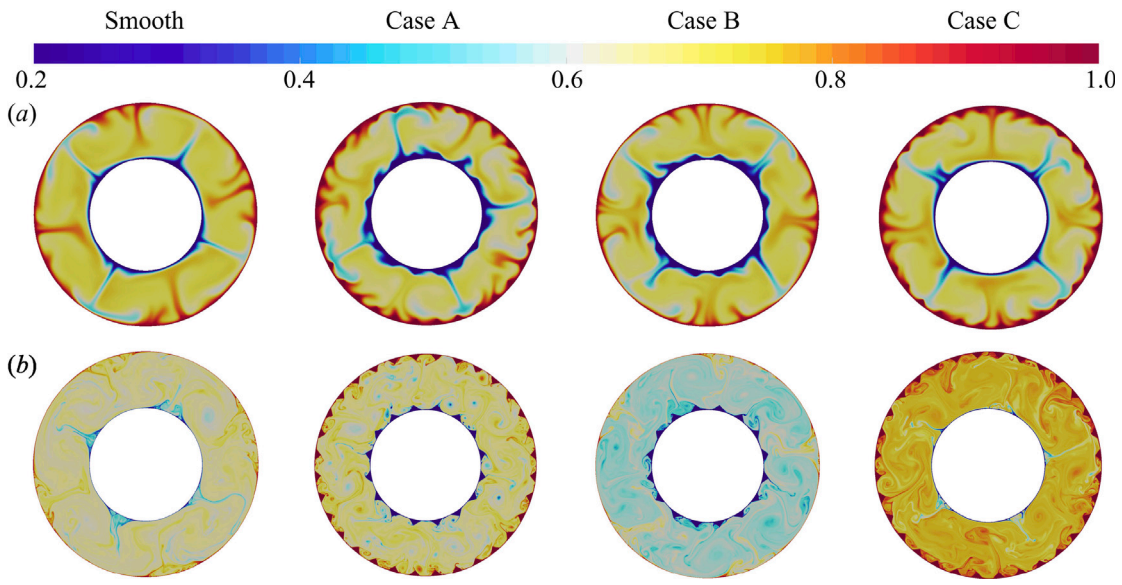

Fig. 2. Instantaneous temperature fields for different cases at $Ra = 10^6$ (*a*) and $Ra = 10^9$ (*b*). Here, the columns from left to right represent the smooth case, Case A, Case B and Case C, respectively. To visualize the plumes clearly, the temperature colourbar is from 0.2 to 1. All figures share the same colourbar.

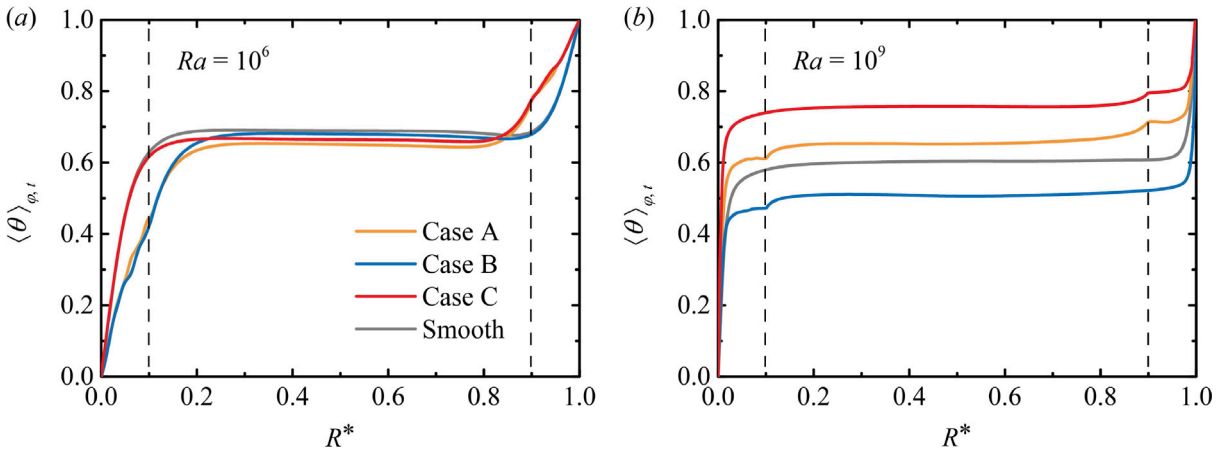

Fig. 3. Azimuthal and time averaged temperature profiles along the dimensionless radial direction $R^* = (R-R_i)/(R_o-R_i)$ for different cases at two Rayleigh numbers $Ra = 10^6$ (*a*) and $Ra = 10^9$ (*b*). The dashed lines donate the top of rough elements.

temperature fields exhibit substantial variations for different combinations of rough walls at large $Ra = 10^9$. According to previous research conducted on classical RBC [32], the interaction between large-scale circulation and rough structures leads to the generation of secondary flows within the gaps of the rough structures. The combined effect of these secondary flows and the large-scale circulation promotes the generation and detachment of plumes, which serve as the primary heat carriers in turbulent convective heat transfer [33]. Consequently, the bulk temperature distribution in Case A, where both walls are rough, is relatively close to that in the smooth case. However, in Case B, where only the inner wall is rough, the bulk temperature distribution exhibits a significantly closer proximity to the temperature set on the inner rough walls compared to the smooth case. Conversely, in Case C, where only the outer wall is rough, the bulk temperature distribution demonstrates a closer resemblance to the temperature set on the outer rough walls compared to the smooth case.

To further substantiate the qualitative analyses conducted earlier, Fig. 3 presents the averaged temperature profiles for different combinations of rough walls and smooth cases at $Ra = 10^6$ (Fig. 3*a*) and $Ra = 10^9$ (Fig. 3*b*). It is worth noting that the average temperature profile for smooth walls in ACRBC exhibits notable asymmetric property in comparison to classical RBC. Which can be attributed to the inherent asymmetry arising from the effects of radially dependent centrifugal buoyancy [7]. Specifically, in the current study with a radius ratio of $\eta = 0.5$, the centrifugal buoyancy at the outer cylinder is twice as strong as that at the inner cylinder. As shown in Fig. 3(*a*), the bulk temperature remains uniform and exhibits similarity regardless of wall roughness at $Ra = 10^6$. However, the temperature gradients near the rough walls are milder compared to those in the smooth cases. This can be attributed to the rough elements being submerged within the thermal BL at this particular *Ra*, causing the detachment of plumes primarily occurring from the roughness tips. Consequently, the temperature near the roughness tips closely matches that of the rough surfaces, resulting in a gentler temperature gradient in the vicinity of the rough walls. Nevertheless, at $Ra = 10^9$, significant variations in bulk temperature are observed for different combinations of roughness, as depicted in Fig. 3(*b*). These quantitative findings further emphasize the influence of wall roughness on temperature distribution in ACRBC, reinforcing the notion that as the Rayleigh number increases, the effect of roughness becomes more pronounced, leading to a bias in the temperature fields towards the values set on the rough walls.

Table 1
Simulation parameters. The columns from left to right indicate the following: different cases, the Rayleigh number Ra, the resolution employed, the maximum grid spacing Δ_g compared with the Kolmogorov scale η_K, the maximum grid spacing Δ_g compared with the Batchelor scale η_B, the calculated Nusselt numbers Nu and their relative difference of two halves ϵ_{Nu}.

Cases	*Ra*	$N_\varphi \times N_r$	Δ_g/η_K	Δ_g/η_B	*Nu*	ϵ_{Nu}
Case A	1.0×10^6	1024 × 128	0.33	0.68	7.46	0.18%
Case A	2.2×10^6	1024 × 128	0.42	0.88	9.36	0.25%
Case A	4.7×10^6	1024 × 128	0.56	1.15	12.51	0.37%
Case A	1.0×10^7	1536 × 192	0.48	0.99	16.23	0.15%
Case A	2.2×10^7	1536 × 192	0.63	1.31	21.53	0.23%
Case A	4.7×10^7	1536 × 192	0.82	1.70	28.54	0.31%
Case A	1.0×10^8	2048 × 256	0.79	1.65	37.13	0.49%
Case A	2.2×10^8	3072 × 384	0.69	1.44	49.53	0.35%
Case A	4.7×10^8	3072 × 384	0.90	1.87	65.92	0.30%
Case A	1.0×10^9	4096 × 512	0.83	1.71	68.55	0.46%
Case A	2.2×10^9	6144 × 768	0.71	1.47	85.52	0.55%
Case A	4.7×10^9	6144 × 768	0.90	1.87	105.15	0.56%
Case B	1.0×10^6	1024 × 128	0.32	0.67	7.32	0.28%
Case B	2.2×10^6	1024 × 128	0.42	0.88	9.19	0.32%
Case B	4.7×10^6	1024 × 128	0.55	1.13	11.76	0.37%
Case B	1.0×10^7	1536 × 192	0.47	0.97	15.05	0.35%
Case B	2.2×10^7	1536 × 192	0.61	1.27	19.34	0.44%
Case B	4.7×10^7	1536 × 192	0.79	1.64	24.68	0.21%
Case B	1.0×10^8	2048 × 256	0.76	1.58	31.42	0.59%
Case B	2.2×10^8	3072 × 384	0.66	1.36	39.93	0.55%
Case B	4.7×10^8	3072 × 384	0.84	1.74	49.61	0.48%
Case B	1.0×10^9	4096 × 512	0.80	1.67	61.62	0.56%
Case B	2.2×10^9	6144 × 768	0.69	1.43	76.95	0.38%
Case B	4.7×10^9	6144 × 768	0.88	1.82	94.14	0.72%
Case C	1.0×10^6	1024 × 128	0.32	0.67	7.32	0.31%
Case C	2.2×10^6	1024 × 128	0.42	0.87	9.07	0.42%
Case C	4.7×10^6	1024 × 128	0.54	1.12	11.18	0.27%
Case C	1.0×10^7	1536 × 192	0.46	0.96	14.03	0.45%
Case C	2.2×10^7	1536 × 192	0.60	1.24	17.75	0.14%
Case C	4.7×10^7	1536 × 192	0.77	1.60	22.75	0.26%
Case C	1.0×10^8	2048 × 256	0.74	1.54	28.81	0.22%
Case C	2.2×10^8	3072 × 384	0.64	1.33	36.14	0.42%
Case C	4.7×10^8	3072 × 384	0.82	1.71	45.83	0.53%
Case C	1.0×10^9	4096 × 512	0.79	1.64	57.31	0.62%
Case C	2.2×10^9	6144 × 768	0.68	1.41	73.16	0.47%
Case C	4.7×10^9	6144 × 768	0.87	1.81	92.08	0.61%
Smooth	1.0×10^6	1024 × 128	0.32	0.67	7.29	0.23%
Smooth	2.2×10^6	1024 × 128	0.42	0.87	8.88	0.17%
Smooth	4.7×10^6	1024 × 128	0.54	1.11	10.91	0.32%
Smooth	1.0×10^7	1536 × 192	0.45	0.94	13.14	0.34%
Smooth	2.2×10^7	1536 × 192	0.59	1.22	16.41	0.29%
Smooth	4.7×10^7	1536 × 192	0.75	1.55	20.26	0.33%
Smooth	1.0×10^8	2048 × 256	0.72	1.49	25.28	0.49%
Smooth	2.2×10^8	3072 × 384	0.62	1.28	31.16	0.75%
Smooth	4.7×10^8	3072 × 384	0.79	1.63	38.37	0.41%
Smooth	1.0×10^9	4096 × 512	0.75	1.56	47.21	0.56%
Smooth	2.2×10^9	6144 × 768	0.64	1.34	58.87	0.67%
Smooth	4.7×10^9	6144 × 768	0.82	1.70	72.21	0.84%

3.2. Heat transport

In the following analysis, the heat transport is systematically investigated as a function of Ra, covering a range spanning more than three orders of magnitude, for both smooth and rough walls in three different cases. As shown in Fig. 4, the results for smooth wall in the present study are in an excellent agreement with those from a previous study [5] that share the same radius ratio. The smooth case exhibits an effective scaling exponent of $\beta = 0.27$, which is close to the typical value observed in two-dimensional RBC [34]. The characteristics of heat transport with increasing Ra for smooth wall have been extensively discussed in prior studies by Jiang et al. [5,11], a prominent finding is that the ultimate regime occurs in ACRBC at a relatively lower Ra (drop from 10^{14} to 10^{11}) compared to classical RBC [19,20].

Now, let us shift our focus to the scenarios involving wall roughness, which exhibit more complex changes. As shown in Fig. 4, the rough surfaces have no effect on Nusselt number (Nu) at the low Rayleigh number $Ra = 10^6$. With increasing Ra, two universal regimes can be identified in Case A and Case B. When the roughness elements protrude through the thermal BL, heat transport experiences a significant enhancement, resulting in local effective scaling exponents of approximately 0.36 and 0.32 for Case A and Case B, respectively. We refer to this as regime I, the enhanced exponent regime. However, further increases in Ra do not extend regime I in the present study. Instead, the scaling exponents for these two cases saturate and fall back to the effective value of $\beta = 0.28$, similar to the smooth case. We refer to this as regime II, the saturated exponent regime. It is worth noting that, despite the decrease in scaling exponents from regime I to regime II, the values of Nu for Case A and Case B still show a increase (as depicted in Table 1). The transition of regimes exhibits a notable contrast compared to smooth ACRBC, where the local effective scaling exponent increases with Ra and is associated with the ultimate regime [11]. Additionally, the transition point between the two regimes with rough surfaces occurs at a much lower Rayleigh number ($Ra = 1.0 \times 10^9$ for Case A and $Ra = 4.7 \times 10^8$ for Case B) compared to the value ($Ra = 1.0 \times 10^{11}$) observed in smooth ACRBC [11]. However, it is important to note that the transition observed in the presence of rough surfaces should not be interpreted for the ultimate transition. The increase in the local effective scaling exponent in regime I is a transitional regime, where the roughness elements start to perturb the thermal BL. This observation aligns with the findings of Zhu et al. [26], who also identified these two regimes in classical RBC with wall roughness, exploring a wide range of Rayleigh numbers and various roughness characteristics.

In regime II, there are differences between Case A and Case B. The Nusselt number of Case A is consistently greater than that of Case B, which can be attributed to the heat transfer enhancement mainly caused by the enlarged surface area of the outer cylinder and the strong plume ejections within these additional cavities. However, in Case C, due to the greater curvature of the outer cylinder compared to the inner cylinder and the roughness on the outer surface, the hot plumes consistently dominate over the cold plumes in this competition. As a result, although the effective scaling exponent for Case C remains at $\beta = 0.30$, which is lower than the values of Case A and B in regime I, it does not saturate under the currently explored parameters. Further investigation is needed to determine if the effective scaling exponent will saturate with further increasing Ra.

In Rayleigh–Bénard convection, it is commonly observed that the rough surfaces become active only when the thickness of the thermal boundary layer is smaller than the characteristic height of the roughness [23,35,36]. Fig. 5(a) illustrates the thermal BL thickness δ_{th} for different wall boundaries normalized by the roughness height δ as a function of the Rayleigh number. Fig. 5(b) shows the ratio of thermal BL thickness for different combinations of roughness compared to the smooth case, also as a function of the Rayleigh number. In our study, we focus on comparing the mean thermal BL thickness changes with Ra for different combinations of rough walls and the smooth case. While there are various methods available to define the thickness of the thermal boundary layer, we choose the widely used formula $\delta_{th} \approx d\sigma/(2Nu)$, where σ is the geometry factor defined as $\sigma = [(Ri + R_o)/(2\sqrt{R_i R_o})]^4$ [37].

As depicted in Fig. 5(a), the non-dimensional thermal boundary layer thickness δ_{th}/δ for all roughness cases is less than 1, indicating that the mean thermal BL thickness is smaller than the height of the roughness elements for the explored parameters and decrease with increasing Ra. However, the heat transport does not immediately been intensified until the Rayleigh number reaches a higher value ($Ra \approx 2.2 \times 10^6$). This can be attributed to the majority of roughness elements being submerged within the thermal BL, with plumes primarily detaching from the roughness tips, resulting in less pronounced heat transport enhancement. Noting that the thermal BL thickness of Case A at $Ra = 4.7 \times 10^8$ is slightly larger than that at $Ra = 1.0 \times 10^9$, although this difference is not clearly visible in Fig. 5(a). In addition, Fig. 5(a) illustrates that the thickness of the thermal boundary layer exhibits

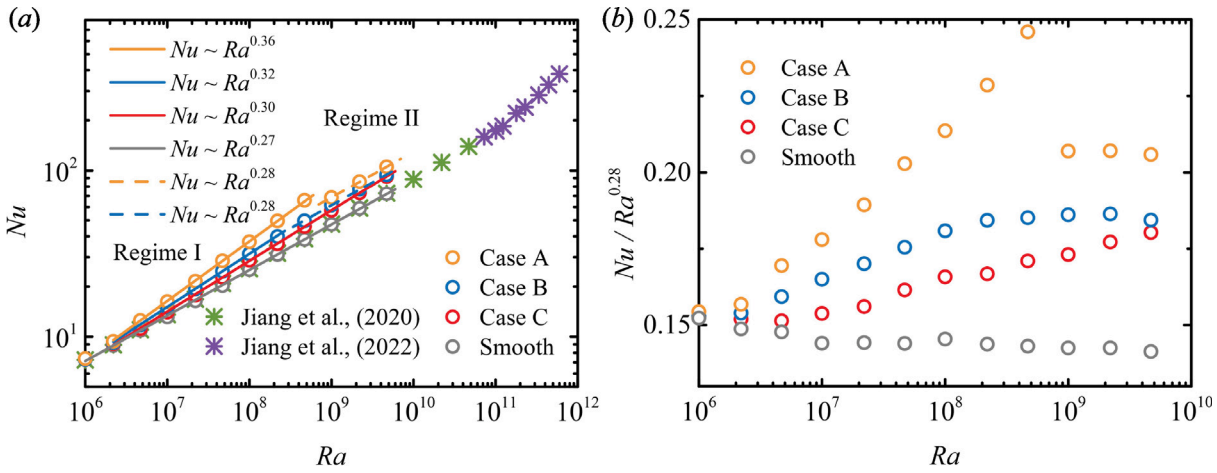

Fig. 4. (*a*) Nusselt number *Nu* as a function of Rayleigh number *Ra* for smooth cases and rough cases with three different combinations at $\eta = 0.5$. Note that the fitted lines for the rough cases begin at $Ra = 2.2 \times 10^6$, indicating the start of regime I. (*b*) The same as (*a*), but now the Nusselt number is scaled with $Ra^{-0.28}$.

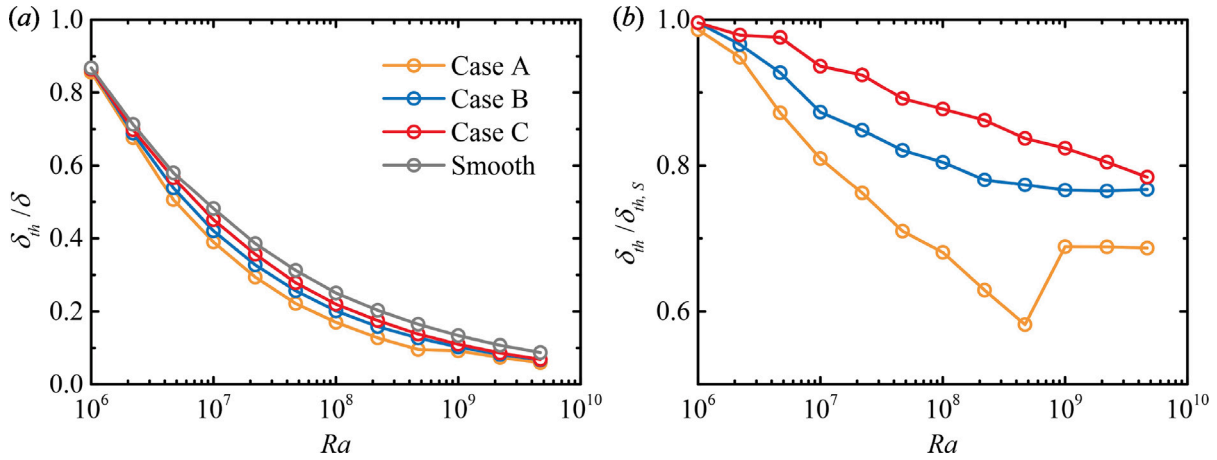

Fig. 5. (*a*) Dimensionless value δ_{th}/δ of the roughness height as a function of the Rayleigh number. Here, δ_{th} donates the estimated thickness of the thermal boundary layer, given by $\delta_{th} \approx d\sigma/2Nu$, where σ is the geometry factor defined as $\sigma = [(R_i + R_o)/(2\sqrt{R_i R_o})]^4$ [37], and δ is the height of roughness element. (*b*) The thermal BL thickness for different combinations of roughness compared to that for smooth case, as a function of the Rayleigh number. $\delta_{th,S}$ represents the thickness of thermal boundary layer for the smooth case.

an ascending order for Case A, Case B, and Case C at the same *Ra*. This indicates that the impact of the roughness elements on the flow dynamics and heat transfer is most pronounced in Case A, followed by Case B, and least significant in Case C (refer to Fig. 4). Fig. 5(*b*) illustrates that the ratio of thermal BL thickness for Case C, compared to the smooth case, decreases as the Rayleigh number (*Ra*) increases. This suggests that the local effective scaling exponent of Case C consistently increase within the explored range of *Ra* when compared to the smooth case. However, the situation becomes more intricate for Case A and Case B. The ratio of Case B initially exhibits a faster decrease compared to Case C, and then stabilizes at higher *Ra* values. Similarly, the ratio of Case A initially decreases at a higher rate than Case B, and then remains constant at high *Ra*. Consequently, the local effective scaling exponents of Case A and Case B, as depicted in Fig. 4, first increase and subsequently converge back to the value similar to the smooth case.

To understand the mechanisms underlying the two regimes, we present temperature profiles and local flow structures inside the cavity regions for Case A at different *Ra* in Fig. 6. At the low $Ra = 1.0 \times 10^6$, the cavity regions exhibit viscosity dominance, resulting in an unaltered Nusselt number (*Nu*) when compared to the smooth case. With increasing *Ra*, secondary vortices generated by large-scale rolls emerge in the cavity regions. In regime I, the weak secondary vortices fail to efficiently mix the fluid within the cavities, leading to a flow primarily governed by viscosity. Consequently, the temperature profile within the cavity appears relatively linear. In regime II, the secondary vortices intensify, inducing smaller vortices, which, in turn, induce even smaller vortices at the centers of the valleys. The intense mixing during this process causes the roughness elements to be covered by a thin thermal BL that is uniformly distributed along the rough surfaces as shown in Fig. 6(*e*), effectively resembling an enlarged surface area, as observed by Zhu et al. [26] in classical RBC. As a result, the mean temperature profile exhibits steepness primarily at the center of the cavities between the roughness elements, while resembling the smooth case elsewhere. These findings also support the notion that, for even higher *Ra* values, the scaling exponent in the rough case may eventually converge to the same value as observed in the smooth case.

3.3. Zonal flow

As reported in the study by Jiang et al. [5], the convection rolls in ACRBC exhibit a prograde rotation around the axis, with a rotation rate faster than the system rotation of the experimental system. This phenomenon is commonly referred to as zonal flow, which has been investigated in experiments of astrophysical and geophysical flows [38, 39]. The mechanism behind zonal flow can be attributed to the influence of Coriolis force, which causes the hot plumes detached from the outer cylinder and cold plumes detached from the inner cylinder to deflect toward their right-hand side from their initial direction, forming

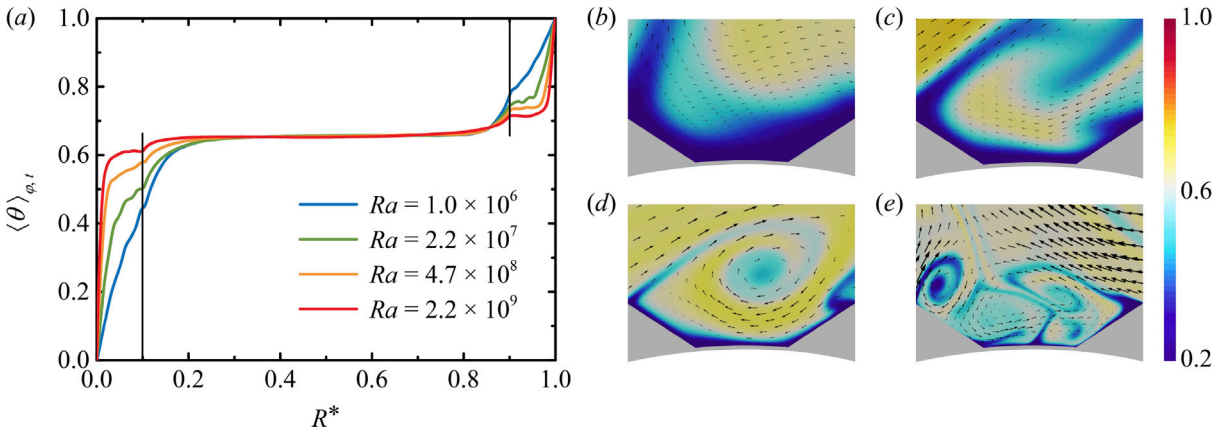

Fig. 6. (*a*) Mean temperature profiles along the radial direction for Case A at (*b*) $Ra = 1.0 \times 10^6$, (*c*) $Ra = 2.2 \times 10^7$ (the middle of regime I), (d) $Ra = 4.7 \times 10^8$ (the end of regime I), and (*e*) $Ra = 2.2 \times 10^9$ (regime II). Figures (*b–e*) show the instantaneous temperature fields, superposed by the velocity vectors in the cavity regions. To visualize the plumes clearly, the temperature colourbar is from 0.2 to 1. Figures (*b–e*) share the same colourbar.

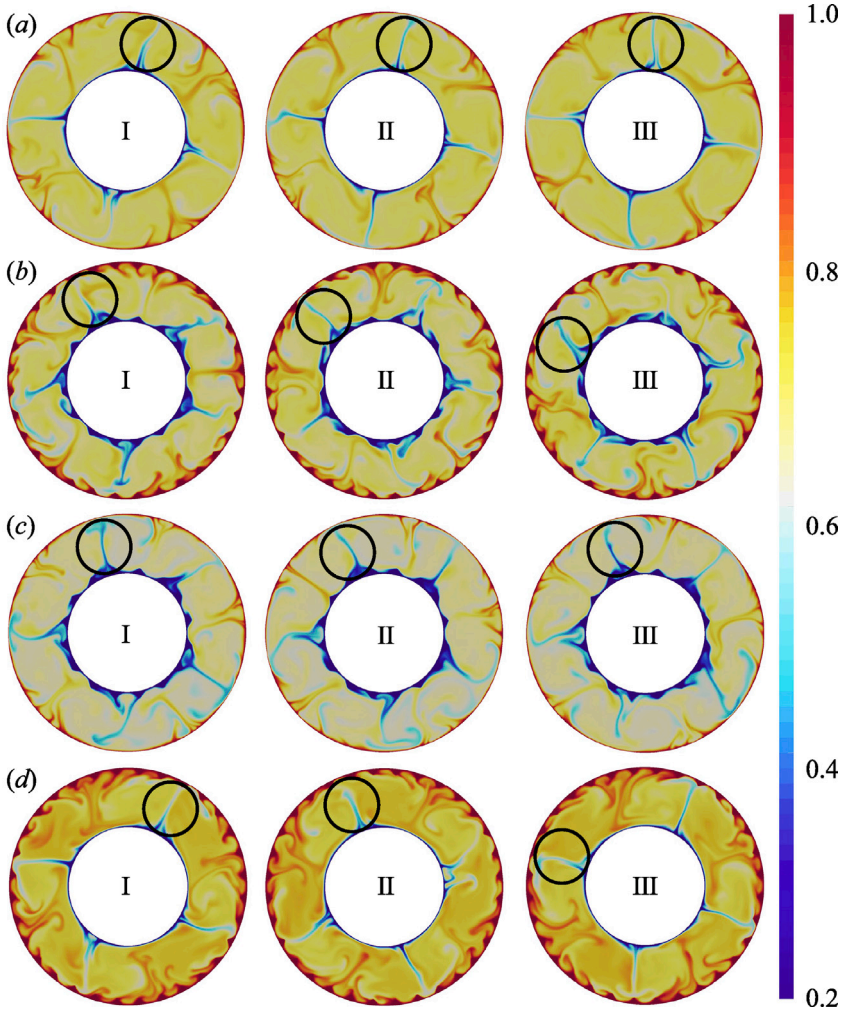

Fig. 7. Snapshots of instantaneous temperature fields at $Ra = 10^7$ for (*a*) smooth case, (*b*) Case A, (*c*) Case B, and (*d*) Case C, the whole system rotates anticlockwise. Roman numerals I, II, and III donate three moments with equal time intervals. To visualize the plumes clearly, the temperature colourbar is from 0.2 to 1. All figures share the same colourbar.

two similar angles when the system rotates anticlockwise. However, due to the different curvatures of the cylinders, the similar deflection angles of the hot and cold plumes result in different effects. The hot plumes directly impact the position where the cold plumes are ejected, leading to the anticlockwise rotation of the cold plumes and the overall flow. On the other hand, the cold plumes does not directly affect the motion of the hot plumes due to the relatively large distance between the ejection position of the hot plumes. Consequently, the hot plumes

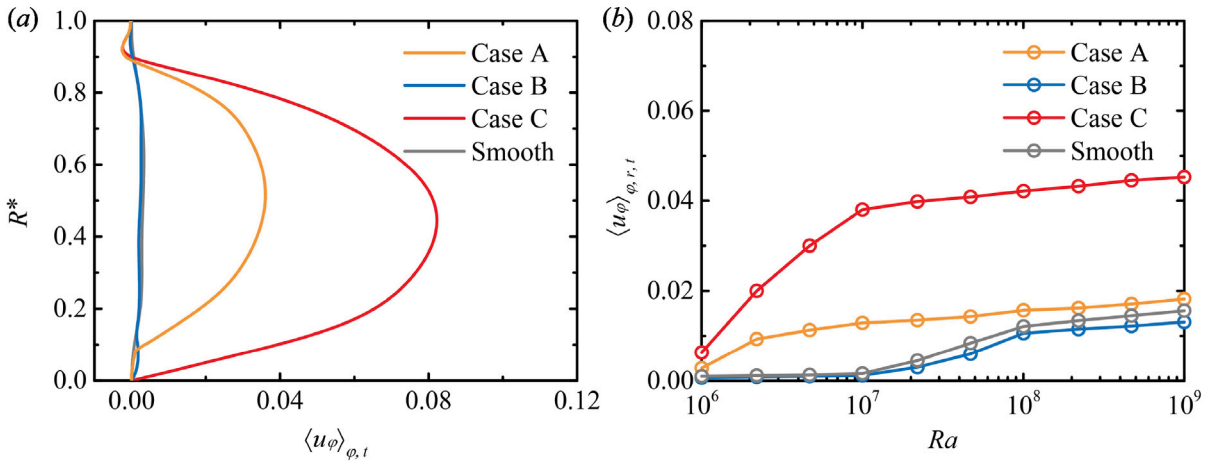

Fig. 8. *(a)* Averaged azimuthal velocity profiles along the radial direction for different wall boundaries at $Ra = 10^7$. *(b)* The azimuthal velocity, averaged over the azimuthal and radial directions as well as time, is plotted for different combinations of roughness as a function of Rayleigh number ranging from $Ra = 10^6$ to $Ra = 10^9$. Due to the time-consuming nature of obtaining statistics for the mean azimuthal velocity, we limit the calculation of the averaged azimuthal velocity up to $Ra = 10^9$.

win and push the overall flow to move in the same direction as the system rotation. Further detailed analysis can be found in our previous studies [5,7].

Fig. 7 displays snapshots of instantaneous temperature fields for three different combinations of rough and smooth surfaces at three moments (marked as I, II, and III) with equal time intervals, all at $Ra = 10^7$. The selection of $Ra = 10^7$ allows for clear visualization of the plumes at this specific *Ra*, and a particular cold plume is highlighted using a black circle. As shown in Fig. 7(*a*), the plume arms in the smooth case at $Ra = 10^7$ remain almost motionless in the azimuthal direction. It was found that the zonal flow observed by Jiang et al. [5] and Wang et al. [7] occurs at $Ro^{-1} = 1$, a value much lower than the $Ro^{-1} = 20$ in the present study. As mentioned above, the emergence of zonal flow in ACRBC results from the interaction between the Coriolis force and the different curvatures of the inner and outer cylinders. At $Ro^{-1} = 1$, which indicates a balance between the Coriolis force and inertial force, the flow operates within the inertial regime. In this regime, the hot plumes dominate the competition with the cold plumes and push the overall flow in the direction of system rotation. However, at a larger value of $Ro^{-1} = 20$, the strong Coriolis force effectively restrains the movement of the flow in the direction of system rotation, causing the convection rolls to remain almost stationary in the azimuthal direction.

The introduction of roughness into the system leads to distinct characteristics, as observed in Figs. 7. In Case B (Fig. 7*c*), where only the inner cylinder is rough, the zonal flow closely resembles that of the smooth case. Conversely, in Case C, where only the outer cylinder is rough, the zonal flow becomes significantly apparent. However, in Case A, where both cylinders are rough, the presence of a pronounced zonal flow is not evident. This phenomenon can be attributed to the roughness promoting the emission of plumes, as noted by Du and Tong [32]. In other words, more hot plumes are generated and detached from the outer rough walls, which exerts a substantial influence, propelling the overall flow in the azimuthal direction despite the strong Coriolis force. When compared to Case C (Fig. 7*d*), the zonal flow in Case A (Fig. 7*b*) is relatively weak due to the resistance posed by the roughness elements on the inner cylinder. Now, let us turn our attention back to Case B, where the outer cylinder is smooth while the inner cylinder is rough. In this configuration, the occurrence of hot plumes originating from the outer wall is relatively reduced compared to Cases A and C. Additionally, the presence of a rough inner wall acts as a barrier, impeding the movement of hot plumes. As a result, the zonal flow remains undetectable.

The radial profiles of averaged azimuthal velocity provide further evidence of the presence of zonal flow, as depicted in Fig. 8. Fig. 8(*a*) displays the averaged azimuthal velocity profiles for different wall boundaries at $Ra = 10^7$. It is observed that the averaged azimuthal velocity is nearly zero for Case B and the smooth case, while it is greater than zero for Case A and Case C. Furthermore, the velocity magnitude for Case C is higher than that for Case A. These findings offer an additional illustration for the existence of zonal flow under different wall boundary conditions at $Ra = 10^7$.

Additionally, Fig. 8(*b*) illustrates the averaged azimuthal velocity as a function of Rayleigh number, ranging from $Ra = 10^6$ to $Ra = 10^9$. It is evident that the averaged azimuthal velocities for different wall boundaries increase with *Ra*. Notably, for Case B and the smooth case, the averaged azimuthal velocities remain close to zero until the Rayleigh number exceeds 10^7. As *Ra* increases, the intensity of the large-scale circulation amplifies, leading to the formation and detachment of plumes. Consequently, the zonal flow becomes more pronounced for Case A and Case C, where the outer walls are rough. Moreover, even in Case B, where the outer cylinder is smooth and the inner one is rough, a discernible zonal flow is observed. The findings presented in Fig. 7 are strongly supported by these quantitative results. Specifically, the presence of roughness on the outer wall encourages the formation of zonal flow, whereas roughness on the inner wall diminishes its strength. These findings may have important implications for controlling heat transfer and flow motion in rapidly rotating machines.

4. Conclusions

In this study, we conducted extensive two-dimensional direct numerical simulations to explore the influence of rough surfaces on annular centrifugal Rayleigh–Bénard convection. The key findings of this investigation can be summarized as follows: Firstly, at low Rayleigh numbers, the rough surfaces have a negligible effect on the temperature fields. However, as the Rayleigh number increases, the influence of roughness becomes more prominent, causing the temperature fields to bias towards the values set on the rough walls. This effect can be attributed to the rough walls promoting the generation and detachment of plumes, which act as the primary heat carriers in turbulent convective heat transfer. Secondly, the impact of rough surfaces on heat transport is also negligible at low Rayleigh numbers. However, as the Rayleigh numbers increase, the influence of different combinations of roughness becomes more pronounced, following a trend of this order (Case A > Case B > Case C) at the same Rayleigh number. Additionally, the presence of wall roughness introduces two universal regimes: in regime I, where roughness elements protrude through the thermal boundary layer, heat transport is significantly enhanced, leading to a significant increase in scaling exponent; in regime II, the scaling

exponent returns to a value similar to the smooth case. The decrease in scaling exponent can be attributed to the intense mixing caused by secondary vortices within the roughness elements, leading to a thin and uniformly distributed thermal boundary layer along the rough surfaces, resembling the behavior observed in the smooth case. Consequently, the effective scaling exponent reaches a saturation point, returning to a value similar to that of the smooth case. Thirdly, the presence of roughness on the outer wall promotes the emergence of zonal flow, while roughness on the inner wall weakens it. These findings provide quantitative evidence for the influence of wall roughness on temperature fields, heat transport, and zonal flow in annular centrifugal Rayleigh–Bénard convection, shedding light on the complex interplay between fluid dynamics, thermal convection, and rough surfaces.

CRediT authorship contribution statement

Fan Xu: Writing – original draft, Visualization, Validation, Software, Methodology, Investigation, Formal analysis, Data curation. **Jun Zhong:** Writing – review & editing, Formal analysis. **Jinghong Su:** Writing – review & editing, Software, Formal analysis. **Bidan Zhao:** Writing – review & editing, Investigation. **Yurong He:** Writing – review & editing, Supervision, Resources, Project administration. **Chao Sun:** Writing – review & editing, Supervision, Project administration, Funding acquisition, Conceptualization. **Junwu Wang:** Writing – review & editing, Supervision, Software, Resources, Project administration, Methodology, Funding acquisition.

Declaration of competing interest

The authors declare that they have no known competing financial interests or personal relationships that could have appeared to influence the work reported in this paper.

Data availability

Data will be made available on request.

Acknowledgments

This study is financially supported by National Natural Science Foundation of China (11988102), Science Foundation of China University of Petroleum, Beijing, China (No. 2462024YJRC008) and the New Cornerstone Science Foundation through the XPLORER prize.

References

[1] G. Ahlers, S. Grossmann, D. Lohse, Heat transfer and large scale dynamics in turbulent Rayleigh-Bénard convection, Rev. Modern Phys. 81 (2) (2009) 503–537.
[2] D. Lohse, K.-Q. Xia, Small-scale properties of turbulent Rayleigh-Bénard convection, Annu. Rev. Fluid Mech. 42 (2010) 335–364.
[3] F. Chillà, J. Schumacher, New perspectives in turbulent Rayleigh-Bénard convection, Eur. Phys. J. E 35 (2012) 1–25.
[4] R.E. Ecke, O. Shishkina, Turbulent rotating Rayleigh-Bénard convection, Annu. Rev. Fluid Mech. 55 (2023) 603–638.
[5] H. Jiang, X. Zhu, D. Wang, S.G. Huisman, C. Sun, Supergravitational turbulent thermal convection, Sci. Adv. 6 (40) (2020) eabb8676.
[6] A. Rouhi, D. Lohse, I. Marusic, C. Sun, D. Chung, Coriolis effect on centrifugal buoyancy-driven convection in a thin cylindrical shell, J. Fluid Mech. 910 (2021) A32.
[7] D. Wang, H. Jiang, S. Liu, X. Zhu, C. Sun, Effects of radius ratio on annular centrifugal Rayleigh-Bénard convection, J. Fluid Mech. 930 (2022) A19.
[8] D. Wang, J. Liu, Q. Zhou, C. Sun, Statistics of temperature and velocity fluctuations in supergravitational convective turbulence, Acta Mech. Sin. 39 (4) (2023) 122387.
[9] J. Zhong, D. Wang, C. Sun, From sheared annular centrifugal Rayleigh-Bénard convection to radially heated Taylor-Couette flow: Exploring the impact of buoyancy and shear on heat transfer and flow structure, J. Fluid Mech. 972 (2023) A29.
[10] J. Zhong, J. Li, C. Sun, Effect of radius ratio on the sheared annular centrifugal turbulent convection, 2024, arXiv preprint arXiv:2402.00779.
[11] H. Jiang, D. Wang, S. Liu, C. Sun, Experimental evidence for the existence of the ultimate regime in rapidly rotating turbulent thermal convection, Phys. Rev. Lett. 129 (20) (2022) 204502.
[12] R. Hide, An experimental study of thermal convection in a rotating liquid, Philos. Trans. R. Soc. A 250 (983) (1958) 441–478.
[13] F.H. Busse, C. Carrigan, Convection induced by centrifugal buoyancy, J. Fluid Mech. 62 (3) (1974) 579–592.
[14] F.H. Busse, C. Carrigan, Laboratory simulation of thermal convection in rotating planets and stars, Science 191 (4222) (1976) 81–83.
[15] M. Auer, F.H. Busse, R.M. Clever, Three-dimensional convection driven by centrifugal buoyancy, J. Fluid Mech. 301 (1995) 371–382.
[16] C. Kang, A. Meyer, H.N. Yoshikawa, I. Mutabazi, Numerical study of thermal convection induced by centrifugal buoyancy in a rotating cylindrical annulus, Phys. Rev. Lett. 4 (4) (2019) 043501.
[17] J. Proudman, On the motion of solids in a liquid possessing vorticity, Proc. R. Soc. Lond. Ser. A Math. Phys. Eng. Sci. 92 (642) (1916) 408–424.
[18] G.I. Taylor, Experiments on the motion of solid bodies in rotating fluids, Proc. R. Soc. Lond. Ser. A Math. Phys. Eng. Sci. 104 (725) (1923) 213–218.
[19] S. Grossmann, D. Lohse, Scaling in thermal convection: A unifying theory, J. Fluid Mech. 407 (2000) 27–56.
[20] X. He, D. Funfschilling, H. Nobach, E. Bodenschatz, G. Ahlers, Transition to the ultimate state of turbulent Rayleigh-Bénard convection, Phys. Rev. Lett. 108 (2) (2012) 024502.
[21] K.-Q. Xia, S. Lam, S.-Q. Zhou, Heat-flux measurement in high-Prandtl-number turbulent Rayleigh-Bénard convection, Phys. Rev. Lett. 88 (6) (2002) 064501.
[22] J.-L. Yang, Y.-Z. Zhang, T.-C. Jin, Y.-H. Dong, B.-F. Wang, Q. Zhou, The-dependence of the critical roughness height in two-dimensional turbulent Rayleigh–Bénard convection, J. Fluid Mech. 911 (2021) A52.
[23] Y. Shen, P. Tong, K.-Q. Xia, Turbulent convection over rough surfaces, Phys. Rev. Lett. 76 (6) (1996) 908–911.
[24] X.-L. Qiu, K.-Q. Xia, P. Tong, Experimental study of velocity boundary layer near a rough conducting surface in turbulent natural convection, J. Turbul. (6) (2005) N30.
[25] O. Shishkina, C. Wagner, Modelling the influence of wall roughness on heat transfer in thermal convection, J. Fluid Mech. 686 (2011) 568–582.
[26] X. Zhu, R.J. Stevens, R. Verzicco, D. Lohse, Roughness-facilitated local 1/2 scaling does not imply the onset of the ultimate regime of thermal convection, Phys. Rev. Lett. 119 (15) (2017) 154501.
[27] M. Sharma, K. Chand, A.K. De, Investigation of flow dynamics and heat transfer mechanism in turbulent Rayleigh-Bénard convection over multi-scale rough surfaces, J. Fluid Mech. 941 (2022) A20.
[28] P. Zhao, J. Xu, W. Ge, J. Wang, A CFD-DEM-IBM method for Cartesian grid simulation of gas-solid flow in complex geometries, Chem. Eng. J. 389 (2020) 124343.
[29] P. Zhao, J. Xu, X. Liu, W. Ge, J. Wang, A computational fluid dynamics-discrete element-immersed boundary method for Cartesian grid simulation of heat transfer in compressible gas–solid flow with complex geometries, Phys. Fluids 32 (10) (2020) 103306.
[30] G. Silano, K. Sreenivasan, R. Verzicco, Numerical simulations of Rayleigh-Bénard convection for Prandtl numbers between 10^{-1} and 10^{4} and Rayleigh numbers between 10^{5} and 10^{9}, J. Fluid Mech. 662 (2010) 409–446.
[31] S. Toppaladoddi, S. Succi, J.S. Wettlaufer, Roughness as a route to the ultimate regime of thermal convection, Phys. Rev. Lett. 118 (7) (2017) 074503.
[32] Y.-B. Du, P. Tong, Turbulent thermal convection in a cell with ordered rough boundaries, J. Fluid Mech. 407 (2000) 57–84.
[33] X.-D. Shang, X.-L. Qiu, P. Tong, K.-Q. Xia, Measured local heat transport in turbulent Rayleigh-Bénard convection, Phys. Rev. Lett. 90 (7) (2003) 074501.
[34] E.P. Van Der Poel, R.J. Stevens, D. Lohse, Comparison between two-and three-dimensional Rayleigh-Bénard convection, J. Fluid Mech. 736 (2013) 177–194.
[35] G. Stringano, G. Pascazio, R. Verzicco, Turbulent thermal convection over grooved plates, J. Fluid Mech. 557 (2006) 307–336.
[36] H. Jiang, X. Zhu, V. Mathai, R. Verzicco, D. Lohse, C. Sun, Controlling heat transport and flow structures in thermal turbulence using ratchet surfaces, Phys. Rev. Lett. 120 (4) (2018) 044501.
[37] H.J. Brauckmann, B. Eckhardt, Direct numerical simulations of local and global torque in Taylor-Couette flow up to Re=30000, J. Fluid Mech. 718 (2013) 398–427.
[38] M. Heimpel, J. Aurnou, J. Wicht, Simulation of equatorial and high-latitude jets on Jupiter in a deep convection model, Nature 438 (7065) (2005) 193–196.
[39] J. Von Hardenberg, D. Goluskin, A. Provenzale, E. Spiegel, Generation of large-scale winds in horizontally anisotropic convection, Phys. Rev. Lett. 115 (13) (2015) 134501.